

Spontaneous Origination of Chirality in Melts of Diblock Copolymers with Rigid and Flexible Blocks

Yu. A. Kriksin^{a,*}, S.-H. Tung^b, P. G. Khalatur^{c,e}, and A. R. Khokhlov^{d,e}

^a Keldysh Institute of Applied Mathematics, Russian Academy of Sciences, Miusskaya pl. 4, Moscow, 125047 Russia

^b Institute of Polymer Science and Engineering, National Taiwan University, Taipei, 10617, Taiwan

^c Nesmeyanov Institute of Organoelement Compounds, Russian Academy of Sciences, ul. Vavilova 28, Moscow, 119991 Russia

^d Faculty of Physics, Moscow State University, Moscow, 119991 Russia

^e Institute of Advanced Energy-Related Nanomaterials, University of Ulm, D-89081 Ulm, Germany

*e-mail: kriksin@nm.ru

Abstract—A self-consistent mean-field computer simulation of ordering in melts of diblock copolymers consisting of flexible and rigid rodlike blocks is performed. A three-dimensional model is considered, and a corresponding algorithm for solving mean-field equations in sequential and parallelized versions is developed. The coexistence of microphase separation and orientational ordering gives rise to the appearance of new types of spatial arrangements. In particular, phases with the cubic symmetry and the morphology of hexagonally arranged chiral cylinders are found. The transition of achiral cylinders to chiral cylinders in the melt of achiral diblock copolymers consisting of rigid and flexible blocks is revealed for the first time. The origination of chirality is due to the presence of rigid blocks in the system and orientational interactions between them. With a decrease in temperature, microphase separation caused by incompatibility of chemically different blocks initially occurs in these systems. As a result, the hexagonally ordered structure in which rigid blocks are concentrated in cylindrical microdomains arises. A further decrease in temperature results in the involution of cylindrical microdomains and the formation of a helical structure. To quantify the degree of chirality, a new pseudoscalar index, depending on the linear-scale parameter for which the chirality is studied, is suggested.

DOI: 10.1134/S1811238213070047

INTRODUCTION

Copolymers consisting of flexible and rigid blocks are a sufficiently common object for microphase-separation studies. They cover the whole range of effects observable during phase separation. The presence of both flexible and rigid blocks in these copolymers complicates the phase behavior of systems consisting of them. On the one hand, regions occupied by flexible and rigid blocks may differ considerably in the characteristic linear scale. On the other hand, the cross coupling of incompatibility of monomers of different chemical natures and orientational interactions of rigid blocks causes the specific character of the formed nanostructures. Therefore, the ordering of these copolymers is accompanied by a wide variety of arising nanostructures and a rich phase behavior.

Recent experimental investigations [1–4] of these types of objects made it possible to obtain interesting morphologies in bulk and thin films. These investigations have motivated computer experiments in order to establish regularities of the formation of nanostructures for the considered class of polymers.

Theoretical investigations of these copolymers with sufficiently exact models are necessary to predict properties of the related materials. During the past decade, the numerical simulation of the phase behav-

ior of copolymer melts and solutions via the self-consistent mean-field (SCF) method has gained widespread acceptance [5, 6]. This method was used in [7–19] for linear diblock and multiblock copolymers, branched copolymers, polyelectrolytes, etc. The SCF method may be applied for a wide range of interactions, including weak, medium, and strong aggregation regimes, where other analytical methods prove to be invalid. Chronologically, the numerical SCF methods for flexible-chain copolymers have been developed within the framework of two approaches: the spectral method and the real-space method. They differ in the procedure of solving the modified diffusion equation, which describes the spatial walks of a flexible polymer chain in the presence of an external field. It turned out that the most efficient method for solving mean-field equations in bulk and in thin films is the pseudospectral method suggested in [20, 21] for polymer-physics problems. The description of rigid blocks of copolymers within the mean-field theory differs from that of flexible blocks owing to the presence of orientational degrees of freedom [6, 11, 12]. Numerical solutions of the corresponding equations for rigid-chain copolymers are computationally time-consuming. It is not surprising that studies that have been published in this field are few and deal with one- and two-

dimensional models [11, 12, 22–26]. Note that the mean-field description is significantly simplified for rigid rodlike blocks. In the present paper, a numerical method based on the field expansion over a trigonometric basis and the use of the fast Fourier transform [27] is suggested for calculation of the contribution of rigid rods to the free energy, thereby making the computational costs comparable with those required for calculation of the contribution of the flexible blocks.

Most studies on the computer SCF simulation of copolymers apply conventional single-processor algorithms. When computational costs become substantial, as, for example, for calculations of copolymers with rigid and flexible blocks, it is necessary to use parallelized algorithms. The parallelized version of the algorithm for solving mean-field equations for flexible-chain copolymers was suggested for the first time in [28]. In our previous paper [27], the sequential and parallelized algorithms for solving mean-field equations for diblock copolymers involving flexible and rigid rodlike blocks were developed. As a result, a three-dimensional model of these diblock copolymers was calculated and new three-dimensional nanostructures were obtained. Note that calculations of three-dimensional, rather than one- and two-dimensional, structures make it possible to arrive at a final conclusion about their stability or metastability. Indeed, various solutions of the mean-field equations may coexist at the same model parameters [11–19]. Solutions corresponding to thermodynamically stable states are revealed among them through free-energy minimization over a set of all solutions in three dimensions. This is why it is so important to find all possible solutions of the mean-field equations at given parameters. In practice, this task proves to be unfeasible owing to excessive computational costs. In this case, consideration is necessarily limited to a set of the most probable candidates, for example, on the basis of the weak-segregation theory [18].

One of the novel results presented here is the existence of a three-dimensional locally chiral hexagonal phase that is formed with a decrease in temperature as a result of the chiral-symmetry-breaking phase transition from a conventional (achiral) hexagonal phase. It should be remembered that an object is considered to be chiral if it cannot be matched to its mirror image via any rotations or translations. Cylindrical micelles in the chiral hexagonal phase are formed by rodlike blocks that twist around the cylinder axis and form a helical motif in it. The helix handedness (right or left) is selected randomly. Note that a chiral nanostructure is formed in a system consisting of achiral molecules. The spontaneous deterioration of chirality in systems of achiral molecules was reported in a number of papers [29–33].

To quantitatively estimate the degree of chirality of a structure, a pseudoscalar chirality index that depends on the characteristic linear scale for which chirality is evaluated was suggested. Note that there is

no most chiral object in the universal sense. The degree of chirality substantially depends on what method is selected to measure it. It was shown in [34] that the chirality criterion may be selected for any irregular tetrahedron in such a way that this particular tetrahedron will be the most chiral tetrahedron with respect to this criterion. Thus, the degree of chirality depends on the applied criterion. It should be stressed that, to be precise, a pseudoscalar cannot be used as the chirality criterion, because it vanishes at a certain nonempty quantity of chiral objects [35]. Nevertheless, the pseudoscalar chirality index is useful for the discovery of certain types of chirality, such as helical structures [36]. In particular, our index is sensitive also to the helical motif that is formed within the hexagonal phase.

MODEL OF MELTS OF DIBLOCK COPOLYMERS WITH RIGID AND FLEXIBLE BLOCKS

Let us consider a melt of n diblock copolymers with degree of polymerization N that consists of flexible and rigid rodlike blocks with mean volume fractions of f and $(1 - f)$, respectively. The statistical-segment lengths for the rods and flexible blocks are denoted a and b , respectively. For simplicity, it is taken that monomers of both types have the same volumes. The model is described in detail in [11]. Therefore, we restrict ourselves to presentation of the free energy and SCF equations to be solved numerically.

Let us introduce orientational tensor matrix field $\mathbf{M}(\mathbf{r})$ that is a conjugate to orientational tensor order parameter $\mathbf{S}(\mathbf{r})$ and write the free energy for the melt of diblock copolymers with flexible and rigid rodlike blocks as

$$\begin{aligned} & \frac{F[\varphi_C, \varphi_R, w_C, w_R, \xi, \mathbf{M}]}{nkT} \\ &= -V^{-1} \int d\mathbf{r} [w_C(\mathbf{r})\varphi_C(\mathbf{r}) + w_R(\mathbf{r})\varphi_R(\mathbf{r}) - \mathbf{M}(\mathbf{r}) : \mathbf{S}(\mathbf{r})] \\ & \quad + V^{-1} \int d\mathbf{r} \chi N(\varphi_C(\mathbf{r}) - f)(\varphi_R(\mathbf{r}) - 1 + f) \quad (1) \\ & \quad - (2V)^{-1} \int d\mathbf{r} \mu N \mathbf{S}(\mathbf{r}) : \mathbf{S}(\mathbf{r}) \\ & \quad + V^{-1} \int d\mathbf{r} \xi(\mathbf{r})(\varphi_C(\mathbf{r}) + \varphi_R(\mathbf{r}) - 1) - \ln Q[w_C, w_R, \mathbf{M}], \end{aligned}$$

where V is the system volume, χ is the Flory–Huggins parameter, and μ is the Maier–Saupe orientational-interaction parameter. Local volume fractions $\varphi_C(\mathbf{r})$ and $\varphi_R(\mathbf{r})$ and their conjugate fields $w_C(\mathbf{r})$ and $w_R(\mathbf{r})$ refer to flexible and rigid blocks, respectively. They describe the spatial distribution and interaction of corresponding monomers. Lagrange factor $\xi(\mathbf{r})$ (the pressure field) provides the condition of melt incompressibility. Energy is measured in kT units, where k is the

Boltzmann constant and T is the absolute temperature.

Expression $Q[w_C, w_R, \mathbf{M}]$ under the natural-logarithm sign is the single-chain configuration integral determined from the equality

$$Q[w_C, w_R, \mathbf{M}] = \frac{1}{4\pi V} \int d\mathbf{r} q(\mathbf{r}, f; w_C) \int d\mathbf{u} \exp \left[- \int_0^{1-f} ds \Gamma(\mathbf{r} + \beta s \mathbf{u}, \mathbf{u}) \right] \quad (2)$$

Here, \mathbf{u} is the unit vector characterizing the current direction of the rodlike block,

$$\Gamma(\mathbf{r}, \mathbf{u}) = w_R(\mathbf{r}) - \mathbf{M}(\mathbf{r}) : \mathbf{U}(\mathbf{u}), \quad (3)$$

$$\frac{\partial}{\partial s} q(\mathbf{r}, s; w_C) = \nabla^2 q(\mathbf{r}, s; w_C) - w_C(\mathbf{r}) q(\mathbf{r}, s; w_C), \quad (4)$$

$$q(\mathbf{r}, 0; w_C) = 1, \quad 0 \leq s \leq f, \quad (5)$$

$$\beta = \frac{\sqrt{6} a N}{b N^{1/2}}, \quad (6)$$

$$\mathbf{U}(\mathbf{u}) = \|u_{\alpha\beta}\| = \left\| u_{\alpha} u_{\beta} - \frac{1}{3} \delta_{\alpha\beta} \right\|, \quad \alpha, \beta = x, y, z. \quad (7)$$

Calculating functional derivatives of free energy (1),

$$\begin{aligned} \frac{\delta F}{\delta w_{\alpha}} = 0, \quad \frac{\delta F}{\delta \xi} = 0, \quad \frac{\delta F}{\delta \mathbf{M}} = 0, \\ \frac{\delta F}{\delta \varphi_{\alpha}} = 0, \quad \alpha = C, R, \end{aligned} \quad (8)$$

we arrive at the self-consistent mean-field equations

$$w_C(\mathbf{r}) = \chi N (\varphi_R(\mathbf{r}) - 1 + f) + \xi(\mathbf{r}), \quad (9)$$

$$w_R(\mathbf{r}) = \chi N (\varphi_C(\mathbf{r}) - f) + \xi(\mathbf{r}), \quad (10)$$

$$\varphi_C(\mathbf{r}) + \varphi_R(\mathbf{r}) = 1, \quad (11)$$

$$\mathbf{M}(\mathbf{r}) = \mu N S(\mathbf{r}), \quad (12)$$

where

$$\varphi_C(\mathbf{r}) = \frac{1}{Q[w_C, w_R, \mathbf{M}]} \int_0^f ds q(\mathbf{r}, s; w_C) \tilde{q}(\mathbf{r}, f - s; w_C), \quad (13)$$

$$\begin{aligned} \frac{\partial}{\partial s} \tilde{q}(\mathbf{r}, s; w_C) = \nabla^2 \tilde{q}(\mathbf{r}, s; w_C) - w_C(\mathbf{r}) \tilde{q}(\mathbf{r}, s; w_C), \\ 0 \leq s \leq f \end{aligned} \quad (14)$$

with the starting condition

$$\tilde{q}(\mathbf{r}, 0; w_C) = \int d\mathbf{u} \exp \left[- \int_0^{1-f} ds \Gamma(\mathbf{r} + \beta s \mathbf{u}, \mathbf{u}) \right]. \quad (15)$$

Equations (4) and (14) are augmented by periodic boundary conditions over space. The volume fraction

of rigid block segments and the orientational-order parameters are defined by the equalities

$$\begin{aligned} \varphi_R(\mathbf{r}) = \frac{1}{4\pi Q} \int d\mathbf{u} \int_0^{1-f} ds q(\mathbf{r} - \beta s \mathbf{u}, f; w_C) \\ \times \exp \left[- \int_0^{1-f} ds' \Gamma(\mathbf{r} + \beta(s' - s) \mathbf{u}, \mathbf{u}) \right], \end{aligned} \quad (16)$$

$$\begin{aligned} \mathbf{S}(\mathbf{r}) = \frac{1}{4\pi Q} \int d\mathbf{u} \mathbf{U}(\mathbf{u}) \int_0^{1-f} ds q(\mathbf{r} - \beta s \mathbf{u}, f; w_C) \\ \times \exp \left[- \int_0^{1-f} ds' \Gamma(\mathbf{r} + \beta(s' - s) \mathbf{u}, \mathbf{u}) \right]. \end{aligned} \quad (17)$$

The model of the melt of diblock copolymers with flexible and rigid blocks is fully described by relationships (1)–(17) underlying the numerical algorithm for solving mean-field equations [27]. Variables with the dimension of length are presented below in units of the gyration radius $R_g = b\sqrt{N}/6$ for a flexible chain of length N .

CHIRALITY INDEX AND ITS CALCULATION

Despite the known disadvantages of pseudoscalars used for quantitative estimations of chirality, the idea of their application for particular objects is attractive. Indeed, if a pseudoscalar is nonzero for a certain object, it takes the opposite value for the mirror object. Therefore, it vanishes for any achiral object. Unfortunately, any pseudoscalar likewise vanishes for a certain class of chiral objects, a circumstance that restricts its application as a universal chirality criterion.

The simplest chiral object in the three-dimensional space is an irregular tetrahedron. In the paper by M.A. Osipov, B.T. Pickup, and D.A. Dunmur [37], a pseudoscalar chirality index (the OPD index) was suggested to describe the degree of molecular chirality on the basis of the weight-average estimation of chirality for all tetrahedrons built of various quadruples of atoms. In addition to the common disadvantages typical of all pseudoscalars, a number of other disadvantages characterize the OPD index, thereby significantly complicating its practical application. Let us enumerate the main disadvantages of the OPD index.

(i) Calculation of this index for an arbitrary object is extremely cumbersome and is practical only for discrete objects with small numbers of points. Indeed, such computations for the assembly of n points require a complete search for all tetrahedrons, and their number is $n(n-1)(n-2)(n-3)/24$. Thus, computational costs grow as $O(n^4)$ with an increase in n .

(ii) According to its construction, the OPD index is the weight-average sum of indices for all possible tetrahedrons arranged within the volume being esti-

mated. However, it ignores the fact that chirality can manifest itself in a different manner on different linear scales. The OPD index gives a certain averaged chirality value for all tetrahedrons of the object if no information on the linear scale at which chirality is exhibited most noticeably.

(iii) The OPD index is proportional to the fourth power of the local density of the object, although it is intuitively clear that objects with proportional densities should have the same chirality indices.

(iv) The OPD index is not invariant with respect to geometrically similar objects.

A new version of the pseudoscalar chirality index free of the aforementioned disadvantages is presented below. The new chirality index may be calculated for any object defined by a local density and is a function of the linear scale of chirality evaluation.

Let $\rho(\mathbf{r}) \geq 0$ be the number-average density of any component (or its volume fraction) and $f(r)$ be the spherically symmetric probability distribution density ($r = |\mathbf{r}|$), satisfying the condition

$$\int f(|\mathbf{r}|)d^3\mathbf{r} = 4\pi \int_0^{+\infty} r^2 f(r) = 1 \quad (18a)$$

$$\langle r \rangle = \int |\mathbf{r}| f(|\mathbf{r}|)d^3\mathbf{r} = 4\pi \int_0^{+\infty} r^3 f(r)dr = 1 \quad (18b)$$

Let us define the chirality index of the linear scale, λ , through the function

$$G(\lambda; f, \rho) = I_1(\lambda; f, \rho)/I_0(\lambda; f, \rho), \quad (19)$$

where

$$I_0(\lambda; f, \rho) = \int d^3\mathbf{r}_1 d^3\mathbf{r}_2 d^3\mathbf{r}_3 d^3\mathbf{r}_4 \rho(\mathbf{r}_1)\rho(\mathbf{r}_2)\rho(\mathbf{r}_3)\rho(\mathbf{r}_4) \times f(\lambda^{-1}r_{12})f(\lambda^{-1}r_{23})f(\lambda^{-1}r_{34}), \quad (20)$$

$$I_1(\lambda; f, \rho) = \lambda^{-7} \int d^3\mathbf{r}_1 d^3\mathbf{r}_2 d^3\mathbf{r}_3 d^3\mathbf{r}_4 \rho(\mathbf{r}_1)\rho(\mathbf{r}_2)\rho(\mathbf{r}_3)\rho(\mathbf{r}_4) \times f(\lambda^{-1}r_{12})f(\lambda^{-1}r_{23})f(\lambda^{-1}r_{34}) \times J([\mathbf{r}_{12}\mathbf{r}_{34}]\mathbf{r}_{14})(\mathbf{r}_{12}\mathbf{r}_{23})(\mathbf{r}_{23}\mathbf{r}_{34}), \quad (21)$$

$$\mathbf{r}_{ij} = \mathbf{r}_i - \mathbf{r}_j, \quad r_{ij} = |\mathbf{r}_{ij}|. \quad (22)$$

Chirality index (19) is characterized as the chirality “charge” (e.g., “left” if it is negative or “right” in the opposite case), corresponding to linear scale λ . Integral (20) plays the role of a normalizing factor. With consideration for (22), we have

$$\mathbf{r}_{14} = \mathbf{r}_{12} + \mathbf{r}_{23} + \mathbf{r}_{34}. \quad (23)$$

Thus, expression $([\mathbf{r}_{12}\mathbf{r}_{34}]\mathbf{r}_{14})(\mathbf{r}_{12}\mathbf{r}_{23})(\mathbf{r}_{23}\mathbf{r}_{34})$ is a polynomial of degree 7 in the nine-dimensional space of variables \mathbf{r}_{12} , \mathbf{r}_{23} , and \mathbf{r}_{34} . Therefore, integral (21) may be

represented as a finite sum with summands of the pattern

$$J = \int d^3\mathbf{r}_1 d^3\mathbf{r}_2 d^3\mathbf{r}_3 d^3\mathbf{r}_4 \rho(\mathbf{r}_1)\rho(\mathbf{r}_2) \times \rho(\mathbf{r}_3)\rho(\mathbf{r}_4)K_1(r_{12})K_2(r_{23})K_3(r_{34}), \quad (24)$$

In each of them, kernels $K_i(r)$ may be analytically calculated or numerically tabulated for given density distributions $f(r)$. Integral (24) is twelvefold, and its direct computation with the use of cubature formulas has extremely high computational costs. However, in the case of periodic structures or in the approximation of periodic boundary conditions, the task of computation of integral (24) may be solved via the fast Fourier transform, as suggested below.

Let

$$[K^* \rho](\mathbf{r}) = \int d^3\mathbf{r}' K(|\mathbf{r} - \mathbf{r}'|)\rho(\mathbf{r}'), \quad (25)$$

then

$$J = \int d^3\mathbf{r}_1 \rho_1(\mathbf{r}_1), \quad (26)$$

where

$$\rho_1(\mathbf{r}_1) = \rho(\mathbf{r}_1)[K_1 * \rho_2](\mathbf{r}_1), \quad (27)$$

$$\rho_2(\mathbf{r}_2) = \rho(\mathbf{r}_2)[K_2 * \rho_3](\mathbf{r}_2), \quad (28)$$

$$\rho_3(\mathbf{r}_3) = \rho(\mathbf{r}_3)[K_3 * \rho](\mathbf{r}_3), \quad (29)$$

The procedure of calculating convolution (25) via the fast Fourier transform is based on the use of the convolution theorem, according to which the convolution of a kernel with density in the real space is transformed into the product of Fourier transforms of the kernel and density. The Fourier transforms of the finite number of kernels $K_i(r_{i,i+1})$, may be calculated analytically or tabulated. Their particular form is determined by probability density $f(r)$ and the seventh-degree monomial terms that enter polynomial $([\mathbf{r}_{12}\mathbf{r}_{34}]\mathbf{r}_{14})(\mathbf{r}_{12}\mathbf{r}_{23})(\mathbf{r}_{23}\mathbf{r}_{34})$.

From the computational viewpoint, it is most suitable to use the Gaussian distribution

$$f(r) = \frac{1}{\sqrt{2\pi}^3} \exp\left(-\frac{r^2}{2\pi}\right), \quad (30)$$

whose normalization is substantiated by equality (18b). In the case of the Gaussian distribution, convolutions (25) may be reduced to the products of one-dimensional convolutions with kernels

$$K(x) \sim x^n \exp\left(-\frac{x^2}{2}\right), \quad n = 0, 1, 2, 3. \quad (31)$$

The calculation of Fourier transforms of kernels (31) is reduced to the differentiation of the characteristic

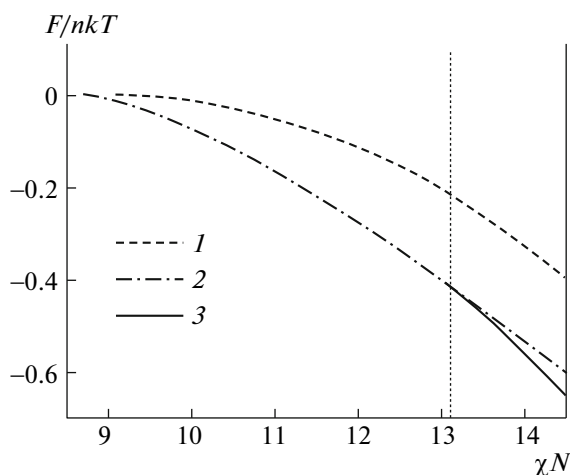


Fig. 1. Free-energy values of (1) lamellar and (2) hexagonal phases as functions of Flory–Huggins parameter χN at $f_c = 0.5$ and $\mu/\chi = 1.3$. At $\chi N = 13.1$, conventional hexagonal phase HEX is transformed into (3) phase HEX* with twisted columnlike microdomains due to the phase transition.

function of a standard one-dimensional normal distribution:

$$F(q) = \exp\left(-\frac{q^2}{2}\right). \quad (32)$$

Let us emphasize some important properties of introduced chirality index (19) following from its definition. The index vanishes identically on one- and two-dimensional objects and on three-dimensional achiral objects. If the index of an object is nonzero, it changes sign in its mirror image but preserves its absolute value. The index takes the same value for objects with densities $\rho(\mathbf{r})$ and $\tilde{\rho}(\mathbf{r})$, respectively, if $\tilde{\rho}(\mathbf{r}) = \text{const}\rho(\mathbf{r})$. For geometrically similar objects ($\tilde{\rho}(\mathbf{r}) = \rho(k\mathbf{r})$), their chirality indices as functions of linear scale λ are related to each other via the similarity transform $G(\lambda; f, \tilde{\rho}) = G(k\lambda; f, \rho)$.

RESULTS AND DISCUSSION

Experimental investigations of copolymer systems with rigid and flexible blocks revealed many interesting morphologies, such as hexagonal stripes, hexagonally arranged cylinders, zigzaglike and wavelike structures, and various lamellar phases [1–4]. Some of these structures were obtained via computer simulations on the basis of one- and two-dimensional self-consistent mean-field models [22–26], but this approach of course does not guarantee that the found structures are thermodynamically stable. An advantage of our iterative algorithms for solving mean-field equations for copolymers with rigid and flexible blocks (including the parallelized version) is the high compu-

tational efficiency, which makes calculations of three-dimensional structures feasible [27].

The parallelized version of the algorithm makes it possible to reach the convergence of iterations for several minutes. This circumstance makes it possible to check hundreds of structures with the use of both random and specially constructed initial iterations as starting conditions [27]. Thus, all potentially possible structures may be divided into two classes. The first class comprises all those structures that were obtained as a result of algorithm iterative convergence, while all the remaining structures, which are considered absolutely unstable within this approach, constitute the second class. As a result, the first class is represented by stable and metastable states. Among the morphologies found through the computer simulation are overwound cylinders (more precisely, columns) on a hexagonal lattice, the zigzaglike phase, truncated polyhedrons in a body-centered lattice, cylinders with almost rectangular cross sections on the square lattice, and mixed and bicontinuous phases.

The most interesting of the aforementioned structures is the twisted column morphology on the hexagonal lattice, which will be referred to as HEX*. This new morphology is stable at a volume fraction of flexible blocks of $f = f_c = 0.5$ and Flory–Huggins parameters in the range $13.1 \leq \chi N < 14.6$. In this case, the ratio of Flory–Huggins and orientational-interaction parameters remains constant: $\mu/\chi = 1.3$. As in [11], the dimensionless length of the rodlike block is selected to be $\beta = 16.33$. The HEX* morphology arises as a result of the phase transition from the usual hexagonal phase (HEX), which is stable in the range $8.8 \leq \chi N < 13.1$ (Fig. 1). A specific feature of this phase transition is that it breaks the chirality of columnlike domains. Usual hexagonal phase HEX appears as a result of the order–disorder phase transition at $\chi N = 8.8$, which is close to that predicted in [38] for the discrete model of diblock copolymers with flexible and rigid blocks in the weak-segregation approximation. Note that $\chi N = 8.8$ is considerably lower than $\chi N = 10.495$ obtained for diblock copolymers with flexible blocks [39], because copolymers with both flexible and rigid blocks are stronger segregated than flexible-chain copolymers under otherwise equal conditions. As seen from Fig. 1, the hexagonal phase has lower free-energy values than those of the lamellar morphology at a volume fraction of flexible blocks of $f_c = 0.5$, despite the fact that the volume fractions of flexible and rigid blocks are equal. This circumstance may be caused by changes in interfaces on the phase diagram that are due to a strongly pronounced conformational asymmetry, as shown in [19] for the melt of amphiphilic diblock copolymers. The mechanism controlling the appearance of curvature in the considered case of equal volume fractions is based on geometrical packing effects related to different volumes occupied by monomers of flexible and rigid

blocks, respectively. Meanwhile, the incompressibility condition requires equal densities on both sides of the boundary between regions enriched with one of the components, a circumstance that leads to preference of the hexagonal phase over the lamellar phase. The calculation results suggest that nonlamellar phases (hexagonal, spherical, etc.) occupy a considerably larger region on the phase diagrams of copolymers with flexible and rigid blocks than that in the conventional case of flexible-chain copolymers. This conclusion agrees with the results of [40]. In addition, it may be expected that nonlamellar morphologies will be gradually replaced with smectic phases of the lamellar type with an increase in ratio μ/χ .

The vertical line $\chi N = 13.1$ (Fig. 1) demarcates regions with the conventional hexagonal morphology, HEX ($\chi N < 13.1$), and the morphology of twisted helical columns, HEX* ($\chi N > 13.1$), where the HEX* morphology has lower free-energy values than those for the usual HEX morphology.

The density-distribution analysis for flexible and rigid blocks shows that nematically ordered columnlike domains become more and more twisted around the cylinder axis with a decrease in temperature (increases in χN and μN). Moreover, flexible blocks are expelled from the columnlike domains to their boundaries.

Let us consider the orientational ordering of rodlike blocks inside columnlike domains. For its analysis, tensor order parameter $\mathbf{S}(\mathbf{r})$ is used. The latter is the second-rank symmetric tensor in the three-dimensional space. As a result of its diagonalization, the triads of its eigenvalues ($\lambda_1(\mathbf{r})$, $\lambda_2(\mathbf{r})$, and $\lambda_3(\mathbf{r})$) and eigenvectors determining the main directions of the orientational ordering may be found. According to [11], scalar orientational-order parameter $3\lambda_{\max}(\mathbf{r})/2$, where $\lambda_{\max}(\mathbf{r})$ is the highest of the three eigenvalues, is a measure of the local orientational ordering, which takes values in the interval [0, 1]. Its highest value corresponds to complete ordering, and its lowest value corresponds to a random orientation. At $\chi N = 14$, the maximum value of the scalar orientational-order parameter in the system is ≈ 0.68 . Figure 2a shows the distribution of the local volume fraction of rigid blocks over the cross-section of the calculated cell, which has a rectangular form with aspect ratio $Y/X = \sqrt{3}$ and is perpendicular to the cylindrical domain axis. Darker regions correspond to the maximum local volume fraction of rigid blocks, and lighter regions correspond to the minimum local volume fraction of rigid blocks. The values of $\lambda_{\max}(\mathbf{r})$ are shown similarly in Fig. 2b. The perpendicular cross-section of columnlike domains has a hexagonal shape. The centers of hexagons form the hexagonal lattice. During a shift of the cross-sectional plane along the domain axes (Fig. 2c), planar regions with the maximum scalar order parameter (hexagons) are synchronously rotated around

these axes. This fact indicates the torsion of the directions along which rodlike blocks are oriented and the formation of helical structures.

This structural motif is clearly seen in Fig. 3a, where the primary eigenvectors of the orientational tensor order parameter are presented. The emergence of the helical motif is related to increases in the degree of segregation and the orientational ordering with a decrease in temperature. The boundaries between different diblock components become sharper. If the monomers of flexible blocks are considered to be spherical, then, at equal densities of spheres and rods in their dense packing, the rods occupy a smaller volume. If a rod were arranged perpendicularly to the interface, a cavity would exist between neighboring rods. This circumstance is in conflict the condition of system incompressibility. Therefore, rods are forced to tilt toward one side in order to avoid overlapping with each other. As a result, columnlike domains with a pronounced helical structure are formed.

A visual description of chiral structures in melts of diblock copolymers with flexible and rigid blocks should be augmented with quantitative estimations of their degrees of chirality. As was noted above, there is no universal chirality measure. In the general case, chiral objects cannot be linearly ordered; in particular, no definite sign (plus or minus) can be assigned to the degree of chirality [35]. In spite of the fact that the idea of the pseudoscalar chirality index is intrinsically self-contradictory and cannot be efficiently applied to all chiral objects, it proves to be useful in a number of particular cases. For example, above-suggested pseudoscalar chirality index (19), like the OPD index [36, 37], is sensitive to the helical motif and may serve as a degree of torsion for a limited class of objects, such as helically twisted cylindrical domains. Linear-scale parameter λ entering index expression (19) makes it possible to reveal the characteristic length at which the chirality is the most noticeable.

In the above numerical experiments with random starting fields, when HEX* hexagonal morphologies arose after the iterative convergence, approximately half of all cylinders are twisted clockwise; the other half are twisted counterclockwise. Note that the effect of the same twisting direction for all domains may be due to a relatively low size of the calculation cell (a number of lattice sites of on the order of 32^3) [27], as is depicted schematically in Fig. 4a. (The rectangular frame shows the cross section of the calculation cell.) The assumption of macroscopic homochirality of a structure requires verification. To this end, additional calculations of the free energy were performed for the hexagonal morphology with an alternating twisting of microdomains (Fig. 4b). This mesophase will be denoted HEX**. Via numerical solution of the mean-field equations, the values of free energy for the homochiral morphology, HEX*, and the morphology with an alternating twisting of microdomains, HEX**, were obtained. They were found to be coincident

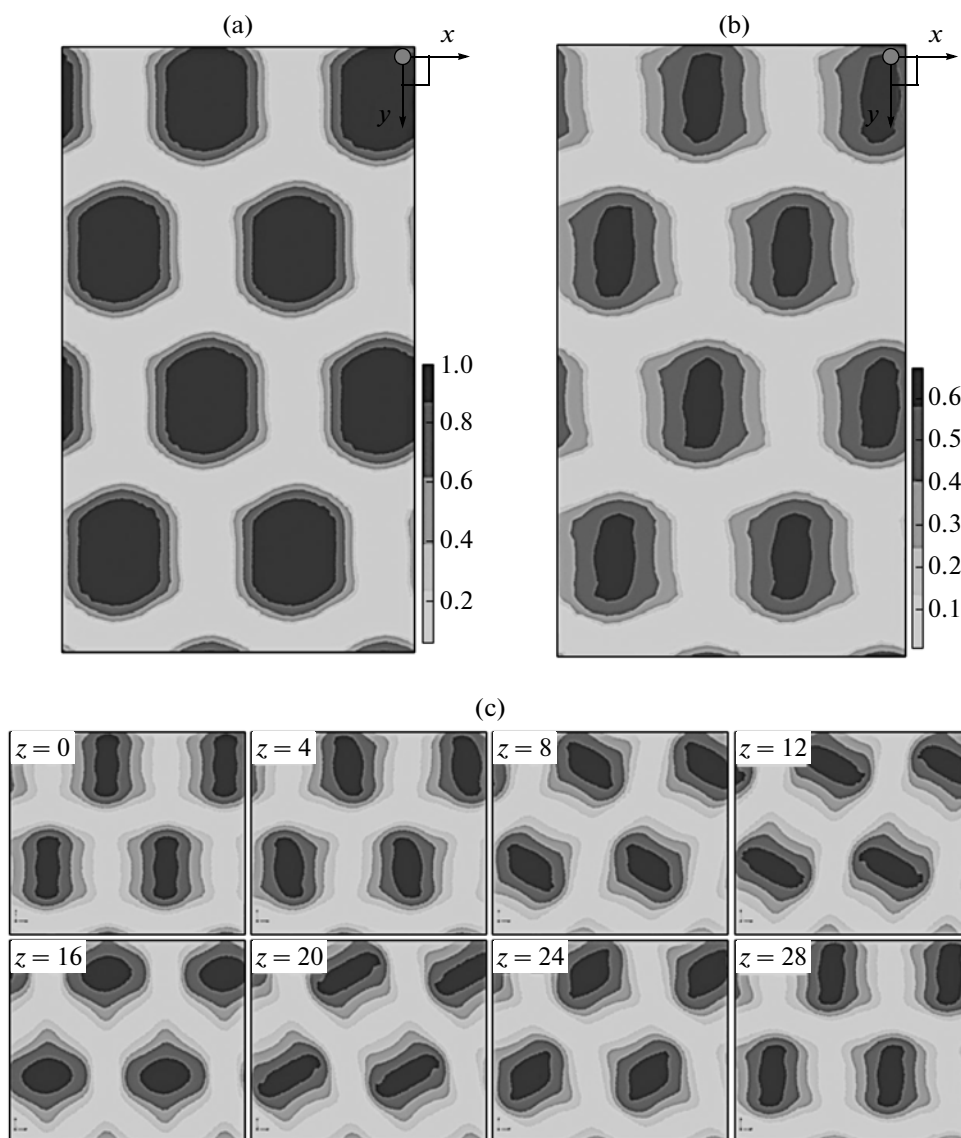


Fig. 2. Distributions of (a) the local volume fraction of rodlike blocks, $\phi_R(\mathbf{r})$, and (b) the local orientational-order parameter, $\lambda_{\max}(\mathbf{r})$, for phase HEX* in the cross section in the XY plane perpendicular to the axes of columnlike microdomains (Z). (c) The orientational-order-parameter distribution in transverse cross sections of various layers Z . The layer number ($z = \eta$) corresponds to the numbering of sites \mathbf{r}_{mn} of a uniform grid in a calculation cell consisting of 32^3 sites along direction Z . Regions predominantly occupied by rigid blocks are darker, while those filled with flexible blocks are lighter.

within the limits of computational accuracy at the same model parameters; that is, they lie on the bold line in Fig. 1. This fact is evidence that columnlike microdomains negligibly weakly interact with each other and can, in principle, have an arbitrary twisting direction. Hence, the hypothesis of a high degree of degeneracy of the ground state represented by the HEX* morphology is plausible. In this case, the macroscopic chirality of an object is not possible in practice, owing to fluctuations.

Let us consider homochiral phase HEX* at various values of parameter χN ($f_c = 0.5$ and $\mu/\chi = 1.3$). The

corresponding curves describing the dependence of index (19) on linear-scale parameter λ are presented in Fig. 5. As is seen from the plots, absolute values of the index grow with an increase in χN . However, the values themselves are conditional because they are normalized weighted sums of chirality indices for an infinite number of tetrahedrons entering the object. They characterize the preponderance of tetrahedrons with one orientational type over those with other types. Therefore, not the values of the index themselves but rather their differences from zero for various values of linear-scale parameter λ are important. The nonzero values of the index provide evidence for the

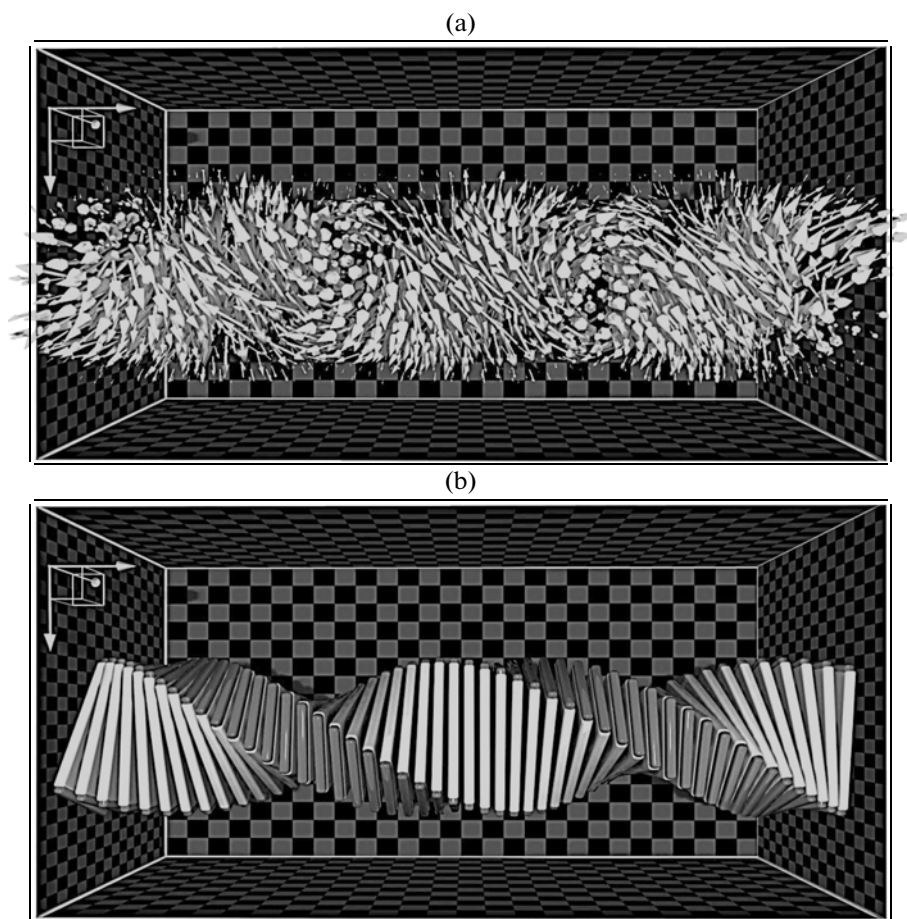


Fig. 3. (a) Orientational ordering in columnlike microdomains of the HEX^* phase. The vector orientation field is given by the primary direction of orientational-order tensor $\mathbf{S}(\mathbf{r})$, the corresponding vector has a length equal to maximum eigenvalue $\lambda_{\max}(\mathbf{r})$, and 8000 vectors are used for the visualization. (b) The schematic illustration of twisting rigid rods in columnlike microdomains.

chirality of the research object on the studied linear scale. The sensitivity of chirality index (19) to the helical type of twisting follows from the helix geometry. Any quadruple of points on the helix on which sequential points are arranged at fixed distances from each other specifies the vertices of congruent tetrahedrons. Therefore, the presence of the helical motif on a sufficiently uniform background leads to the numerical preponderance of tetrahedrons of a certain type, as indicated by nonzero values of the index.

It may be concluded from the curves presented in Fig. 6 that the contrast of the helical motif of columnlike microdomains increases with a decrease in temperature (i.e., with increases in χN and μN). This effect is the most vivid in Fig. 6a, where the dependence of the global-extremum position on χN is presented. An increase in the value of χN from 13.1 to 13.8 is accompanied by an insignificant increase in linear-scale parameter λ . A further increase in χN exerts almost no effect on the global-extremum position, a result that is evidence for the saturation and

fixation of the characteristic dimensions of the structure. At the same time, the absolute global-extremum value increases almost linearly with an increase in χN (Fig. 6b). This phenomenon is related to the strengthening of segregation between flexible and rigid blocks, which is accompanied by an increase in the sharpness of boundaries between regions occupied by flexible and rigid blocks. In particular, the helical motif becomes more contrasted.

Let us analyze the chirality of the morphology with the alternating twisting of microdomains, HEX^{**} (Fig. 4b). For this purpose, let us consider the elementary cell with the shape of a rectangular parallelepiped with dimensions X , Y , and Z ($Y = \sqrt{3}X$) containing two columnlike microdomains with opposite twisting directions. In contrast to homochiral morphology HEX^* , chirality index (19) vanishes on it for all χN values in the interval [13.1, 14.5]. The zero value of the chirality index is provided by the mutual cancellation of contributions from the oppositely twisted micro-

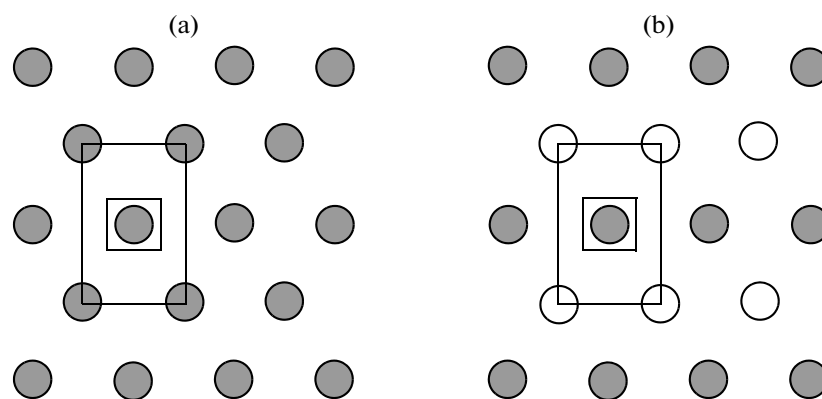


Fig. 4. Schematic representation of the twisting direction of rigid rods in the (a) HEX^* and (b) HEX^{**} phases. Dark microdomains are twisted clockwise, light microdomains are twisted counterclockwise, the rectangular region denotes the calculation cell, and the square indicates the truncated cell used for estimation of the corresponding microdomain twisting.

domains. In spite of this circumstance, the HEX^{**} morphology remains locally chiral in the sense that the twisting of each microdomain may be revealed via calculations of chirality index (19) in a truncated cell containing it. (The truncated-cell region is denoted in Fig. 4 by a square in the center of the calculation cell.) The truncated-cell dimensions were chosen as $X_c = Y_c = X/2$ and $Z_c = Z$ in order to include the whole microdomain into it, on the one hand, and to isolate this microdomain from the neighboring oppositely twisted microdomain, on the other hand. The chirality index in the truncated cell was calculated for both oppositely twisted microdomains of the HEX^{**} morphology.

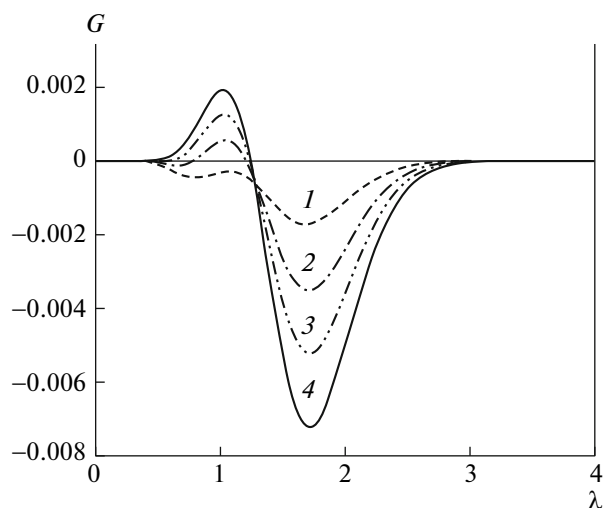


Fig. 5. Chirality index G for the HEX^* morphology as a function of spatial-scale parameter λ defined in the calculation cell (compare Fig. 4) at $\chi N = (1)$ 13.3, (2) 13.7, (3) 14.1, and (4) 14.5; $f_C = 0.5$, and $\mu/\chi = 1.3$.

In Fig. 7, the corresponding curves of chirality index (19) are shown for the values of $f_C = 0.5$, $\chi N = 14$, and $\mu/\chi = 1.3$. The elementary-cell dimensions were $X = 12.20$, $Y = 21.12$, and $Z = 14.56$. The curves depicted in Fig. 7 by dashed and dash-dotted lines correspond to the oppositely charged microdomains and are mirror images of each other with respect to the horizontal axis. On the other hand, the calculation of the chirality index in similar truncated cells for homochiral morphology HEX^* shows that the corresponding curves of the index (the solid line) coin-

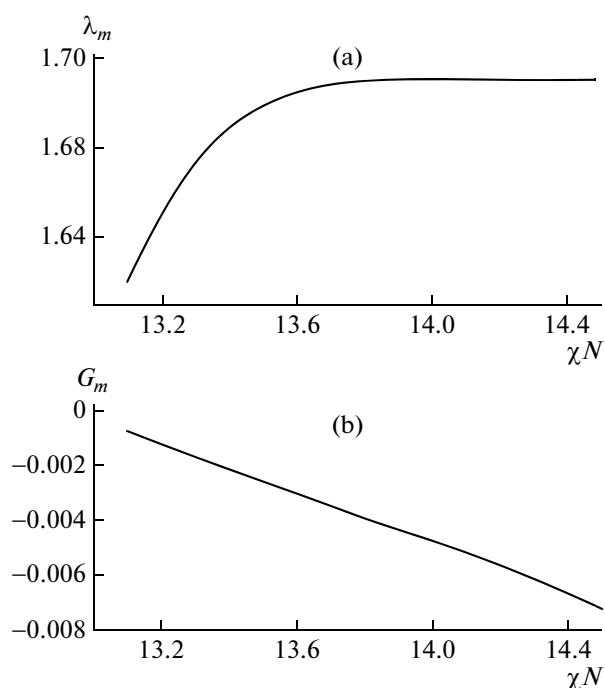


Fig. 6. (a) Position of global extremum λ_m of the chirality index and (b) its value G_m as a function of parameter χN ($f_C = 0.5$, and $\mu/\chi = 1.3$).

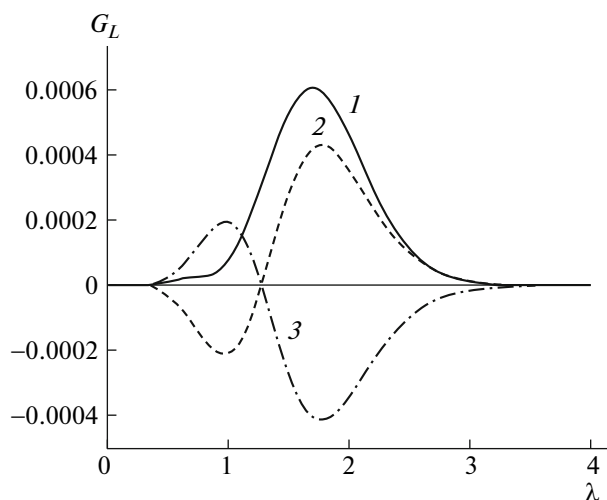


Fig. 7. Local chirality index G_L of a columnlike microdomain as a function of spatial-scale parameter λ for (1) HEX* and (2, 3) HEX** morphologies calculated in the corresponding truncated cells (compare Fig. 4).

side for different microdomains. A certain mismatch in the shapes of the solid and dashed curves in Fig. 7 is explained by the fact that the HEX* and HEX** morphologies have some fine differences in the transition region between different microdomains.

The difference between the chirality-index curves for truncated cells in Fig. 7 and those calculated on the elementary cell (Fig. 6) is due to the application of periodic boundary conditions to the truncated cell. These conditions distort the density field of the origi-

nal solution beyond the limits of the truncated cell. However, it is necessary to apply them in order to provide the chirality-index calculation (19) for a reasonable time.

Let us consider other three-dimensional solutions of mean-field equations for diblock copolymers with rigid and flexible blocks, while putting aside the question on the stabilities of the corresponding morphologies, and calculate chirality indices (19) for them. At model-parameter values of $f_C = 0.75$, $\chi N = 20$, and $\mu/\chi = 2.2$, a body-centered cubic (bcc) morphology for which the elementary cell is a cube with the side $X = Y = Z = 8.42$ was found. Rigid blocks are packed into micelles, but, in contrast to the surfaces of flexible-chain copolymers, the surfaces of the same volume fraction of rigid blocks (Fig. 8a) considerably deviate from the spherical shape and resemble a regular octahedron with smoothed vertexes and sides. Rigid blocks are predominantly directed from the center of a micelle toward its boundary (Fig. 8b). Chirality index (19) vanishes for the bcc morphology, an outcome that is expectable because this morphology is achiral owing to the symmetry of its microdomains.

Another example of the three-dimensional morphology is a binary gyroid. The morphology of the binary gyroid (Fig. 9a) may be found at low values of the dimensionless length of the rodlike block. (In calculations, $\beta = 1$.) The maximum values of the scalar orientational-order parameter (Fig. 9b) are localized in micellelike regions, where the primary directions of the orientational tensor order parameter are shown by lines. The remaining parameters are as follows: $f_C = 0.65$, $\chi N = 20$, and $\mu/\chi = 1.15$. Despite the fact

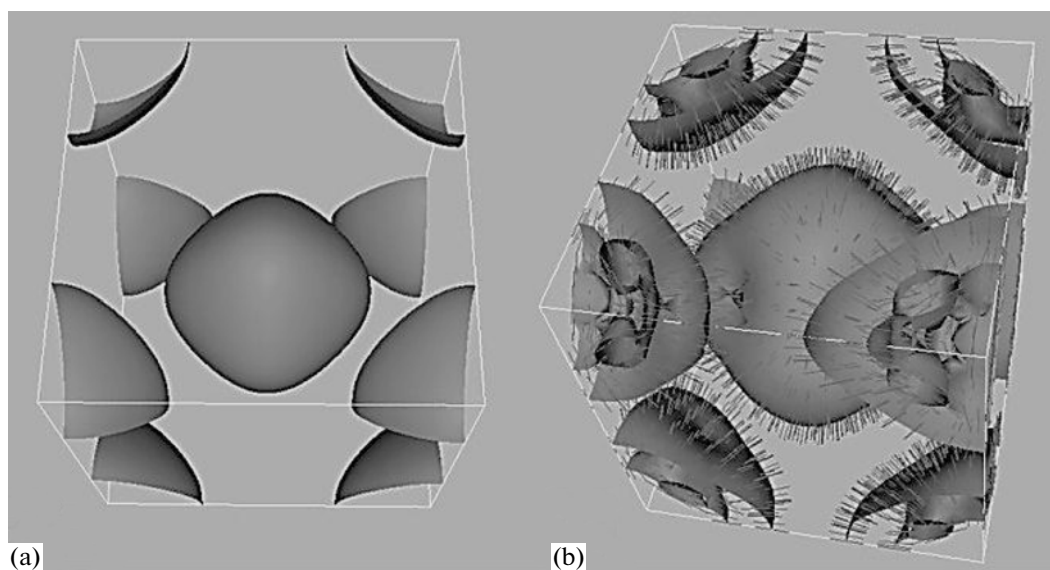


Fig. 8. Constant-level surfaces for (a) the local fraction of rodlike blocks ($\phi_R(\mathbf{r}) = 0.5$) and (b) the local orientational-order parameter ($\lambda_{\max}(\mathbf{r}) = 0.04$) for the bcc phase in the cubic calculation cell: $f_C = 0.75$, $\chi N = 20$, $\mu/\chi = 2.2$, and $\beta = 16.33$. The primary directions of orientation of rigid blocks are shown by lines.

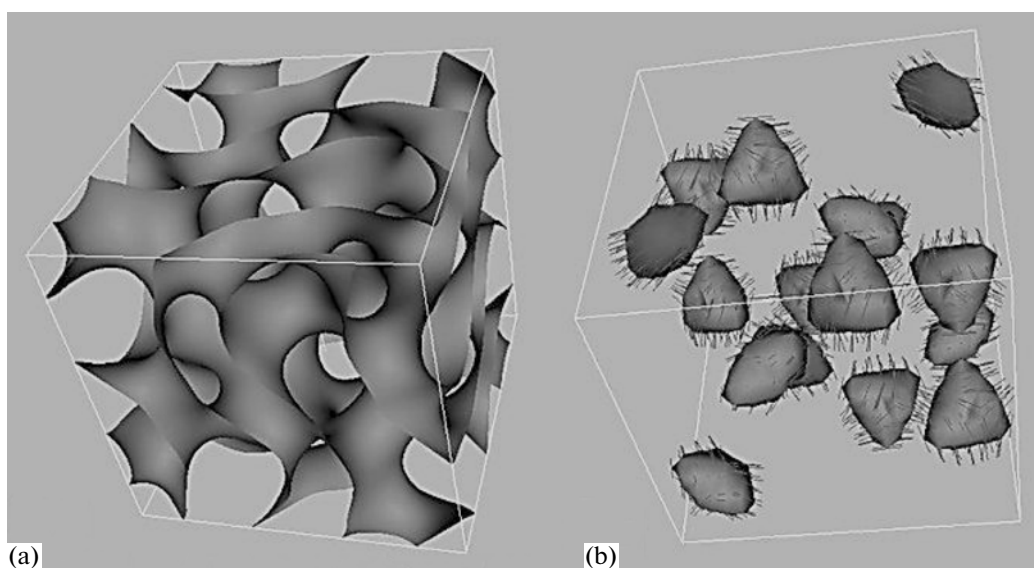


Fig. 9. Constant-level surfaces for (a) the local fraction of rodlike blocks ($\varphi_R(\mathbf{r}) = 0.5$) and (b) the local orientational-order parameter ($\lambda_{\max}(\mathbf{r}) = 0.04$) for the binary-gyroid phase: $f_C = 0.65$, $\chi N = 20$, $\mu/\chi = 1.15$, and $\beta = 1.0$. The primary directions of orientation of rigid blocks are shown by lines.

that the binary-gyroid morphology is necessarily chiral [41], the values of index (19) turn out to be zero. The latter example shows that the use of the same pseudoscalar for quantitative description of various types of chirality may be inefficient. For every type of chirality, quantitative criteria corresponding to its specific features should be employed.

CONCLUSIONS

In order to correctly describe the morphologies formed by copolymers with flexible and rigid blocks owing to microphase separation and orientational ordering, self-consistent mean-field computer simulations should be performed in three dimensions on spatial lattices with a large number of sites. Indeed, if the model were two-dimensional, the cylinder-twisting effect would not be found. In addition, an insufficiently fine grid could lead to a loss of accuracy and to marked distortion of the obtained morphologies. With increases in the dimensions of the simulated system and enhancement of the spatial resolution, the computations become extremely cumbersome and require large computer RAM capacities. Therefore, there is a need to perform parallelized computations with the use of the corresponding algorithms. In the present paper, in the system of copolymers with flexible and rigid blocks, structure formation has been studied on the basis of this approach.

As a result of the self-organization of these copolymers, spontaneous symmetry-breaking occurs: Cylindrical microdomains consisting of rigid blocks are twisted around the cylinder axis and form the helical motif. The direction of microdomain twisting is cho-

sen randomly by the system. Although chirality may not manifest itself at the macroscopic level, the fact that locally chiral structures arise from achiral molecules on the microscopic scale is extremely nontrivial.

Chiral structures should be evaluated not only visually but also quantitatively. In spite of the fact that the degree of chirality for an arbitrary object cannot be described by the universal criterion, it is necessary to develop particular criteria designed for the registration of certain types of chirality, such as the helical motif. In the present paper, a pseudoscalar functional that may be efficiently computed for a periodic object specified by the local density as a function of continuous coordinates has been suggested. This functional depends on the parameter of the linear scale on which the chirality is evaluated. It has been used to reveal chiral structures with the helical motif in the object.

ACKNOWLEDGMENTS

This work was supported by the Russian Foundation for Basic Research and the German Academic Exchange Service (DAAD).

REFERENCES

1. H.-S. Sun, C.-H. Lee, C.-S. Lai, H.-L. Chen, S.-H. Tung, and W.-C. Chen, *Soft Matter* **7**, 4198 (2011).
2. C.-H. Lee and S.-H. Tung, *Soft Matter* **7**, 5660 (2011).
3. J.-C. Chen, C.-L. Liu, Y.-S. Sun, S.-H. Tung, and W.-C. Chen, *Soft Matter* **8**, 526 (2012).
4. Q. Wang, *Soft Matter* **7**, 3711 (2011).

5. G. H. Fredrickson, V. Ganesan, and F. Drolet, *Macromolecules* **35**, 16 (2002).
6. G. H. Fredrickson, *The Equilibrium Theory of Inhomogeneous Polymers* (Oxford Univ. Press, New York, 2006).
7. R. R. Netz and M. Schick, *Phys. Rev. Lett.* **77**, 302 (1996).
8. M. W. Matsen and C. Barrett, *J. Chem. Phys.* **109**, 4108 (1998).
9. W. Li and D. Gersappe, *Macromolecules* **34**, 6783 (2001).
10. D. Duches and D. E. Sullivan, *J. Phys.: Condens. Matter* **14**, 12189 (2002).
11. V. Pryamitsyn and V. Ganesan, *J. Chem. Phys.* **120**, 5824 (2004).
12. M. Shah, V. Pryamitsyn, and V. Ganesan, *Macromolecules* **41**, 218 (2008).
13. W. Song, P. Tang, H. Zhang, Y. Yang, and A.-C. Shi, *Macromolecules* **42**, 6300 (2009).
14. G. Yang, P. Tang, Y. Yang, and Q. Wang, *J. Phys. Chem. B* **114**, 14897 (2010).
15. W. Song, P. Tang, F. Qiu, Y. Yang, and A.-C. Shi, *Soft Matter* **7**, 929 (2011).
16. J. Gao, W. Song, P. Tang, and Y. Yang, *Soft Matter* **7**, 5208 (2011).
17. W. Song, P. Tang, F. Qiu, Y. Yang, and A.-C. Shi, *J. Phys. Chem. B* **115**, 8390 (2011).
18. Yu. A. Kriksin, I. Ya. Erukhimovich, P. G. Khalatur, Yu. G. Smirnova, and G. Brinke, *J. Chem. Phys.* **128**, 244903 (2008).
19. Yu. A. Kriksin, P. G. Khalatur, I. Ya. Erukhimovich, G. Brinke, and A. R. Khokhlov, *Soft Matter* **5**, 2896 (2009).
20. K. O. Rasmussen and G. Kalosakas, *J. Polym. Sci., Part B: Polym. Phys.* **40**, 1777 (2002).
21. G. Tzeremes, K. O. Rasmussen, T. Lookman, and A. Saxena, *Phys. Rev. E: Stat. Phys., Plasmas, Fluids, Relat. Interdiscip. Top.* **65**, 041806 (2002).
22. M. V. Matsen and C. Barret, *J. Chem. Phys.* **109**, 4108 (1998).
23. J.-Z. Chen, C.-H. Zhang, Z.-Y. Sun, Y.-S. Zheng, and L.-J. An, *J. Chem. Phys.* **124**, 104907 (2006).
24. Q.-Y. Tang and Y. Q. Ma, *J. Phys. Chem. B* **113**, 10117 (2009).
25. W. Song, P. Tang, H. Zhang, Y. Yang, and A. C. Shi, *Macromolecules* **42**, 6300 (2009).
26. W. Song, P. Tang, F. Qiu, Y. Yang, and A.-C. Shi, *J. Phys. Chem. B* **115**, 83190 (2011).
27. Yu. A. Kriksin and P. G. Khalatur, *Macromol. Theory Simul.* **21**, 382 (2012).
28. S. W. Sides and G. H. Fredrickson, *Polymer* **44**, 5859 (2003).
29. P. B. Kohl and D. L. Patrick, *J. Phys. Chem. B* **105**, 8203 (2001).
30. Y. Hatwalne and M. Muthukumar, *Phys. Rev. Lett.* **105**, 107801 (2010).
31. P. Chen, X. Ma, P. Duan, and M. Liu, *Chem. Phys. Chem.* **7**, 2419 (2006).
32. M. A. Horsch, Z. L. Zhang, and S. C. Glotzer, *Phys. Rev. Lett.* **5**, 056105 (1995).
33. V. A. Ermilov, V. V. Vasilevskaya, and A. R. Khokhlov, *Vysokomol. Soedin., Ser. A* **52**, 466 (2010).
34. A. Rassat and P. W. Fowler, *Chem.-Eur. J.* **10**, 6575 (2004).
35. P. W. Fowler, *Symmetry: Cult. Sci.* **16**, 321 (2005).
36. M. P. Neal and M. Solymosi, *J. Chem. Phys.* **119**, 3567 (2003).
37. M. A. Osipov, B. T. Pickup, and D. A. Dunmur, *Mol. Phys.* **84**, 1193 (1995).
38. M. Mueller and M. Shick, *Macromolecules* **29**, 8900 (1996).
39. L. Leibler, *Macromolecules* **13**, 1602 (1980).
40. M. Reenders and G. Brinke, *Macromolecules* **35**, 3266 (2002).
41. K. Große-Brauckmann, *Exp. Math.* **6**, 33 (1997).

Translated by A. Yakimanskii